CHALMERS
UNIVERSITY OF TECHNOLOGY

Influence of annealing on enhancing soft magnetic properties in laser powder bed fusion processed Hiperco (Fe-49Co-2V)

Additive Manufacturing Letters 9 (2024) 100208

Contents lists available at ScienceDirect

Additive Manufacturing Letters

journal homepage: www.elsevier.com/locate/addlet

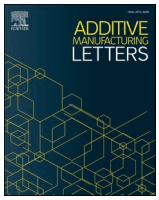

Short Communication

Influence of annealing on enhancing soft magnetic properties in laser powder bed fusion processed Hiperco (Fe-49Co-2V)

S.M. Varahabhatla [a,b], V. Chaudhary [c], Abhishek Sharma [b], S.A. Mantri [a,b], S.S. Joshi [a,b], R.V. Ramanujan [d], Narendra B. Dahotre [a,b], R. Banerjee [a,b,d,*]

[a] Center for Agile and Adaptive Additive Manufacturing (CAAAM), University of North Texas, Denton 76207, TX, USA
[b] Department of Materials Science and Engineering, University of North Texas, Denton, 76207, TX, USA
[c] Industrial and Materials Science, Chalmers University of Technology, Gothenburg SE-41296, Sweden
[d] School of Materials Science and Engineering, Nanyang Technological University, 639798, Singapore

ARTICLE INFO

Keywords:
Fe-Co-2V (Hiperco)
Additive manufacturing
Laser powder bed fusion
Magnetic properties
B2 ordering

ABSTRACT

Annealing of laser powder bed fusion (LPBF) processed Fe-49Co-2 V (Hiperco) samples at 865 °C for 4 h leads to a substantial improvement in its soft magnetic properties. While the as built LPBF samples exhibited relatively higher coercivities (H_c) ranging from 25.8 – 26.5 Oe, the annealed LPBF samples showed significantly lower coercivities (H_c) of 6.9 – 10.8 Oe. These lower H_c values can not only be attributed to the 15–20 times larger grain sizes, but also the higher degree of B2 ordering in the annealed condition. The enhanced degree of B2 ordering also increases the saturation magnetization (M_s), from 213 to 228 emu/g, in samples processed with a laser fluence (energy/density) of 3.4 J/mm^2. These results reveal the underlying mechanisms leading to an enhancement of soft magnetic properties in LPBF processed Hiperco via annealing-induced microstructural control.

Introduction

In the last decade, electric vehicle adoption has experienced an exponential increase. The maximum efficiency of electric motor technology is achieved by minimizing the losses in the motor stators and rotors. Fe-Co alloys are being utilized as stators and rotors in high performance electrical machines due to their high saturation magnetization (M_s), Curie temperature (T_c), permeability (μ) and low coercivity (H_c) characteristics, which reduce energy losses [1–6]. In general, the magnetic properties of bulk Fe-Co alloys are greatly influenced by their microstructure and structural ordering [7,8]. The shape of the magnetic hysteresis loop, coercivity, and relative permeability are influenced by microstructural parameters such as grain size, crystal defects, and crystallographic texture. Especially, structural ordering is known to affect the lattice constant, the average magnetic moment per atom, and the spatial arrangement of atoms [9–11].

According to the Grain Size Dependence of Coercivity and Permeability (GSDCP) theory, the lattice parameter, magneto-crystalline anisotropy, and average grain size (D) of soft magnetic materials influence the coercivity and initial permeability [12–18]. Defect-free large equiaxed grains and higher lattice constant are thus essential for achieving soft (lower H_c) magnetic behavior in Fe-Co alloy [13,14]. Nevertheless, the equiatomic Fe-Co alloys exhibit brittle mechanical behavior, which makes it challenging to fabricate bulk electromagnetic components using conventional manufacturing techniques like rolling, forging, and casting [19–21] . The formation of the ordered B2 phase has been determined as the cause of the brittleness observed in equiatomic Fe-Co alloys [22].

To enhance ductility of Fe-Co alloys while maintaining good magnetic properties, vanadium is added as an alloying element in small amounts (<3 wt%) [23]. The Fe-49Co-2 V (Hiperco) alloys can be manufactured by mechanical alloying and powder rolling, however, post-processing is challenging due to evolution of the ordered B2 phase during low cooling rates [9,10,22,24]. Laser-based additive manufacturing (AM) techniques inherently associated with high cooling rates (>10^3 K/s) can avoid formation of the undesirable ordered B2 phase [1,25]. Such high cooling rates can alter the ordering in various AM processes. The optimum microstructure and magnetic properties can be achieved by a selecting suitable AM manufacturing technique, optimized AM process parameters, and applying appropriate post AM

* Corresponding author.
E-mail address: rajarshi.banerjee@unt.edu (R. Banerjee).

https://doi.org/10.1016/j.addlet.2024.100208
Received 20 January 2024; Received in revised form 5 April 2024; Accepted 9 April 2024
Available online 12 April 2024

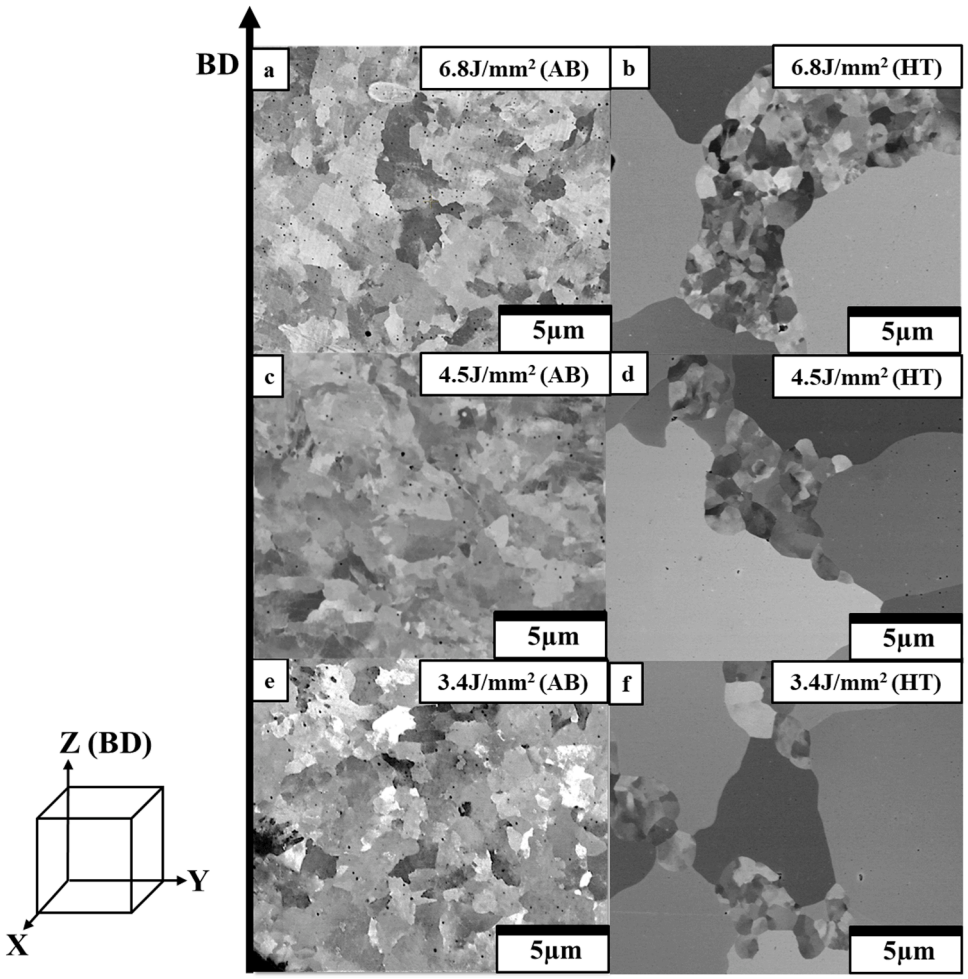

Fig. 1. SEM images on YZ plane of LPBF (a) 6.8 J/mm^2, (b) 4.5 J/mm^2, (c) 3.4 J/mm^2 as-built (AB) conditions and (d) 6.8 J/mm^2, (e) 4.5 J/mm^2, (f) 3.4 J/mm^2 annealed/Heat-treated (HT) conditions.

process heat treatments [25–27]

Recent studies have shown that LPBF and Direct Energy Deposition (DED) are promising AM techniques to print Fe-49Co-2 V alloys [3–5, 28–31]. Nartu et.al [33]successfully fabricated a Fe-49Co-2 V alloy using the DED technique. They observed an improved soft magnetic performance after a two-step annealing heat treatment. The improved soft magnetic performance was attributed to larger grain sizes and the extent of ordering of the B2 phase. The soft magnetic properties of Fe-Co-2 V prepared by DED were comparable to those of wrought Fe-Co-2 V alloys [30]. In the interest of process parameter optimization, Everhart et.al[29] used the LPBF technique to fabricate Fe-49Co-2 V samples, followed by various heat treatment procedures. Although the heat-treated LPBF Fe-49Co-2 V exhibited significant improvement in the saturation magnetization, the coercivity failed to follow the expected trend with the changes in grain size. Tuomas et.al [31] investigated the effect of various heat treatment procedures on the magnetic properties of LPBF deposited Fe-49Co-2 V alloy. They reported improved magnetic properties after heat treatment. However, the influence of laser parameters on the microstructure was not explored in detail.

In the present work, initially the LPBF Fe-49Co-2 V was built using optimized laser process parameters. The post LPBF heat treatment was performed as per the ASTM standard A801 (865 °C, 4 hrs). Typically, LPBF processed Fe-49Co-2 V exhibits higher H_c than wrought Fe-49Co-2 V. However, the previous reports [2,25,29–33] states than annealing can substantially reduce H_c. This paper specifically focuses on underlying mechanisms during annealing that lead to enhanced soft magnetic properties like H_c and M_s of LPBF processed Fe-49Co-2 V.

Materials and methods

The LPBF Trumpf TruPrint 1000 system was utilized to print the three-dimensional builds in the current work. Pre-alloyed Hiperco powders from Carpenter were procured. These spherical powders exhibit D_{10}, D_{50} and D_{90} values of 17, 26 and 51 µm, respectively. A SS 316 L steel seed substrate with 99 mm diameter was used to print these builds. Fe-49Co-2 V cubes of dimensions 10 × 10 × 10 mm^3 were printed using a Trumpf fiber laser source of a wavelength of 1.070 µm. Input parameters such as a laser beam spot diameter of 0.055 mm, a hatch spacing of 0.06 mm, a layer thickness of 0.05 mm, a laser power of 150 W and three different scan speeds (400 mm/s, 600 mm/s, and 800 mm/s) were used to fabricate these cubes. A bi-directional scan strategy with a 90° rotation between each subsequent layer was employed. The oxygen level inside the chamber was maintained below 100 ppm to avoid oxidation of the samples. The LPBF processed conditions are categorized based on their laser fluences (energy per unit area), as summarized in Table. S1. The relative density values of samples processed using laser fluences of 6.8 J/mm^2, 4.5 J/mm^2 and 3.4 J/mm^2, are 98.5 %, 97.5 %, and 97 % respectively.

Subsequently, the substrates containing the builds were removed from the chambers, and the builds were then separated from the substrate across the build direction using a KENT USA (WSI-200) wire electric discharge machine (EDM). Following this step, the samples were prepared for characterization and magnetic measurements. X-ray diffraction (XRD) measurements were carried out at a speed of 1°/min and a step size of 0.025° on all samples using a Rigaku Ultima III XRD

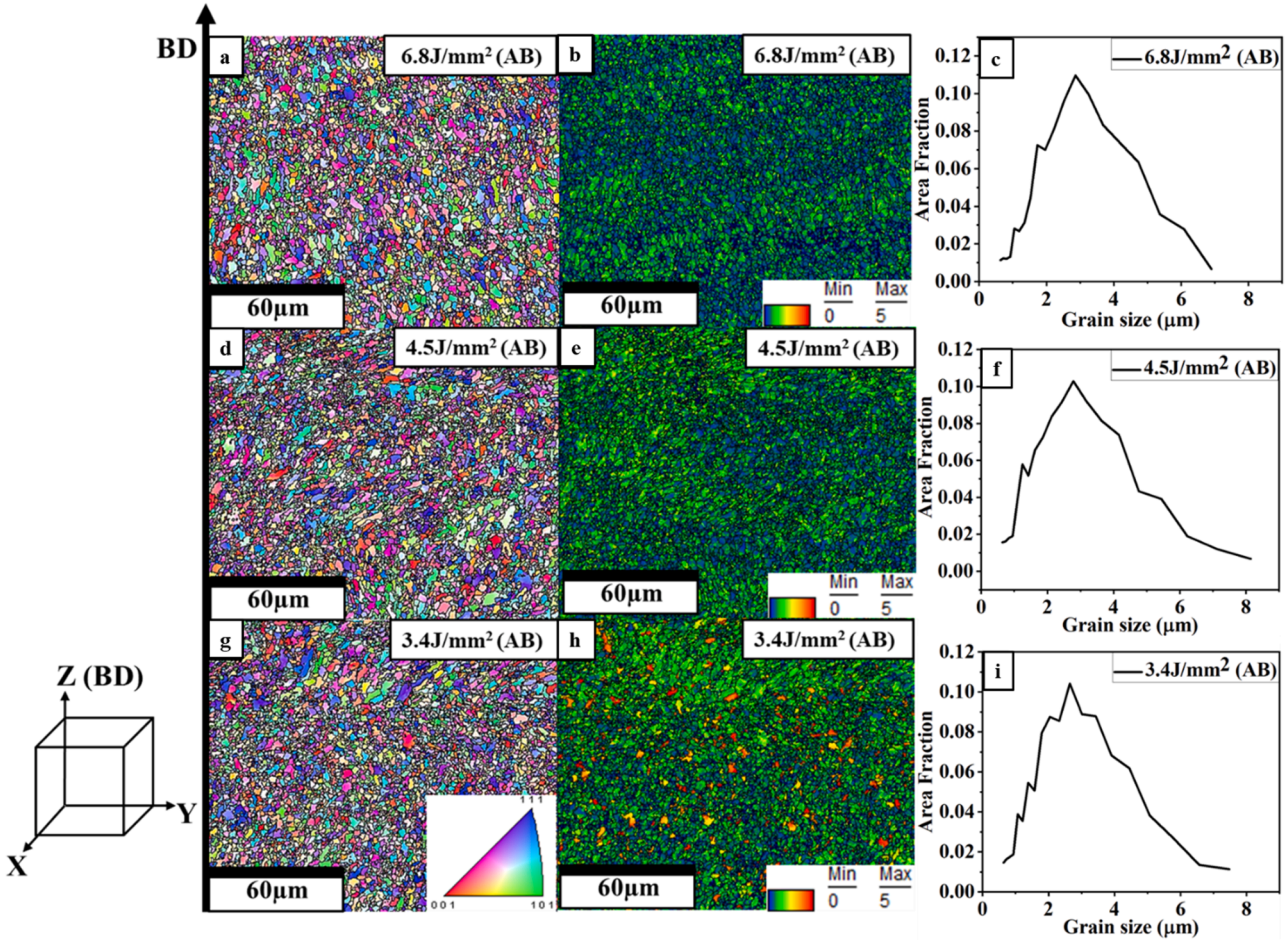

Fig. 2. IPF maps on YZ plane of LPBF processed FeCoV (a) 6.8 J/mm^2, (d) 4.5 J/mm^2 and (g) 3.4 J/mm^2 as-built (AB) conditions. KAM maps of LPBF (b) 6.8 J/mm^2, (e) 4.5 J/mm^2 and (h) 3.4 J/mm^2 as-built conditions.

machine. The MDI Jade software was employed for XRD analysis. A Nova Nano SEM equipped with an electron backscattered diffraction (EBSD) detector was used to investigate the microstructure. The EBSD data were processed using the TSL OIM™ software to produce texture plots and Inverse Pole Figures (IPF). The magnetic properties at room temperature were measured with a Lakeshore 8600 Series Vibrating Scanning Magnetometer (VSM) with a magnetic field of 15kOe. The magnetic field step utilized in the hysteresis loop is 1 Oe, with an averaging time and resolution of 10 s and 1 mOe respectively. Initially, the VSM system was calibrated with a nickel sphere, which detects a magnetic moment of 6.92 emu at an applied magnetic field of 5 kOe. For transmission electron microscopy (TEM), foils were prepared using a dual-beam focused ion beam milling equipment (FEI Nova 200 Nanolab FIB/SEM). The detailed TEM analysis for these foils were performed using an EDS detector-equipped FEI Tecnai G2 F20 ST TEM, which operates in both scanning and transmission modes.

Results and discussion

The backscatter SEM image of the Fe-49Co-2 V pre-alloyed powders used for the LPBF technique is presented in supplementary Fig. S1 (a). The XRD analysis of the powders and the as built LPBF samples (on the XY plane as shown in the Fig. S1 (c)) exhibited peaks corresponding to a single BCC phase with a random texture, as shown in supplementary Fig. S1 (b). The SEM micrographs of both as built and annealed conditions of these LPBF samples, viewed along the X-axis (YZ plane) reveal a single-phase BCC microstructure as shown in Fig. 1. In the as built condition, the backscatter SEM images demonstrate a uniform distribution of columnar and equiaxed grains, for 6.8 J/mm^2, 4.5 J/mm^2 and 3.4 J/mm^2 laser fluences, as shown in Figs. 1(a), (c), and (e). The corresponding backscatter images after annealing exhibited a distribution of largely recrystallized grains with a small fraction of non-recrystallized grains, as shown in Figs. 1(b), 1(d), and 1(f).

EBSD analysis was performed on both the as built and annealed conditions. The grain sizes from the inverse pole figure (IPF) maps (Figs. 2(a), (d), and (g)) appeared to be very fine, with no significant crystallographic texture. The average grain sizes in the built conditions are ~3 µm, as shown in the grain size-area fraction plots (Figs. 2(c), (f) and (i)). The kernel average misorientation (KAM) maps in Figs. 2(b), (e) and (h) correspond to a point-to-point average misorientation between 0° to 5° within the grains represented in the map. This average point-to-point misorientation appears to increase with greater laser scan speed or decreasing laser fluence, possibly due to the increasingly rapid thermo-kinetics associated with increasing scanning speed, which leads to increasingly reduced laser-material interaction times, and hence increasingly shorter time for the grains to evolve with reduced misorientations.

Since the cooling rates are directly proportional to the scanning speeds ($dT/dt \propto V$) [30,34], the average misorientations/dislocation densities are higher for larger scanning speed/lower laser fluence conditions, e.g.., in the case of the laser fluence of 3.4 J/mm^2 as compared to 6.8 J/mm^2. While KAM maps don't directly reflect the residual stresses, they have often been discussed as a qualitative indication of residual stresses [35–39]. Therefore, it is possible that the residual stresses are higher in the sample processed using a laser fluence of 3.4 J/mm^2 as compared to the one processed using 6.8 J/mm^2. Furthermore, EBSD

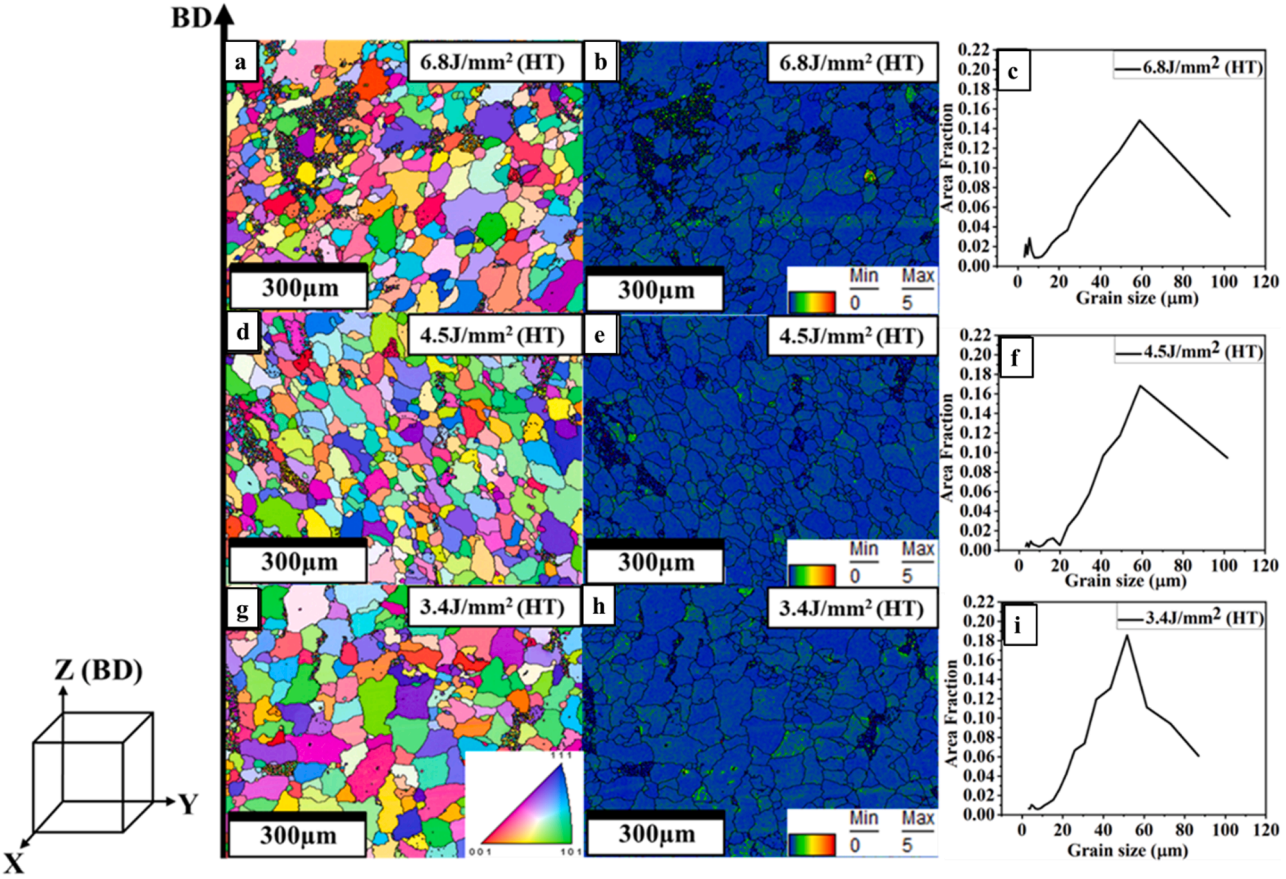

Fig. 3. IPF maps on YZ plane of post heat treated LPBF processed FeCoV (a) 6.8 J/mm^2, (c) 4.5 J/mm^2 and (e) 3.4 J/mm^2 annealed/Heat-treated (HT) conditions. KAM maps of LPBF (b) 6.8 J/mm^2, (d) 4.5 J/mm^2 and (f) 3.4 J/mm^2 Heat-treated (HT) conditions.

analysis was performed on the annealed conditions to analyze average point-to-point misorientations and the grain sizes.

The inverse pole figure maps in Fig. 3(a), (d), and (g), acquired from the same set of LPBF samples after annealing, show a majority fraction of recrystallized grains with a small fraction of non-recrystallized grains. The average grain size of the non-recrystallized grains and the recrystallized grains range from 2 to 3 µm and 50–60 µm, respectively (Figs. 3 (c), (f), and (i)). After the annealing step, the variation in the average misorientations within the recrystallized grains is substantially lower, as revealed by the KAM maps shown in Figs. 3(b), (e) and (h). While the area fraction of the non-recrystallized grains varied from 4 % - 11 % depending on the sample and the region scanned, overall, this fraction was very low as compared to the fraction of recrystallized grains.

VSM measurements were carried out on the LPBF as built and annealed conditions to measure the magnetic properties. The magnetization M(emu/g) versus applied magnetic field H(Oe) hysteresis curves are presented in Fig.4. The saturation magnetization (M_S) and coercivity (H_c) values of the as built conditions range between 213 and 217 emu/g, and 25.8–26.5 Oe, respectively. The annealed conditions showed M_s and H_c values ranging between 228 and 231 emu/g and 6.8–10.8 Oe, respectively.

These magnetic properties are summarized in Table 1. The coercivity values appear to be similar for all the as built conditions. This can be attributed to the similar grain sizes in the case of samples processed using the three different laser fluences. Herzer [12]established that H_c is proportional to D^{-1}, where D is a grain diameter, for grain sizes greater than 600 nm. As the average grain size of all three as built conditions is ~ 3 µm, the coercivities are similar. Firdosy et al. [30]. and Nartu et al. [32] showed a similar trend of H_c proportionate to the D^{-1} in the case of DED processed Fe-49Co-2 V alloys.

A substantial reduction in coercivity was observed for all three samples after annealing. The coercivities of samples built with fluences of 6.8 J/mm^2, 4.5 J/mm^2, and 3.4 J/mm^2 reduced from 25.8 Oe, 26 Oe, and 26.5 Oe to 6.9 Oe, 8.8 Oe, and 10.8 Oe, respectively. This substantial decrease in coercivity can be largely attributed to the increase in the average grain size from 3 µm to 55 µm. Although there is a substantial reduction in coercivity, the values remain relatively higher than those of commercially wrought processed Fe-49Co-2 V (H_c ~ 1.3 Oe) [9] . The lower coercivity values in case of conventionally processed Fe-49Co-2 V can be attributed to their larger grains sizes 75–100 µm [5], substantially larger than ~55 µm observed in case of the annealed LPBF samples. Additionally, the small fraction of the non-recrystallized grains retained in the annealed conditions of the LPBF samples, could also lead to an increase in the H_c as compared to conventionally processed Hiperco.

There is only a marginal difference between the saturation magnetization (M_s) values for all three as built conditions. However, post annealing, the M_s increased substantially for samples processed with all three laser fluences. For example, the M_s increases from 213 emu/g to 228 emu/g in the case of the sample processed using a laser fluence of 3.4 J/mm^2. The underlying rationale for such a substantial increase in M_s via annealing was investigated by characterizing the state of B2 ordering in this alloy. TEM diffraction analysis has been performed on the sample processed using a fluence of 3.4 J/mm^2, for both as built and annealed conditions. Figs. 5(a), and (c) show the selected area electron diffraction (SAED) patterns corresponding to the [001] BCC zone axis (ZA) obtained for the as built, and annealed conditions, respectively. In the case of the as-built sample, there appeared to be very weak (low intensity) {010} type superlattice reflections, one of which has been marked with the circle in the diffraction pattern shown in Fig. 5(a). Such {010} type superlattice reflections can be attributed to B2 ordering

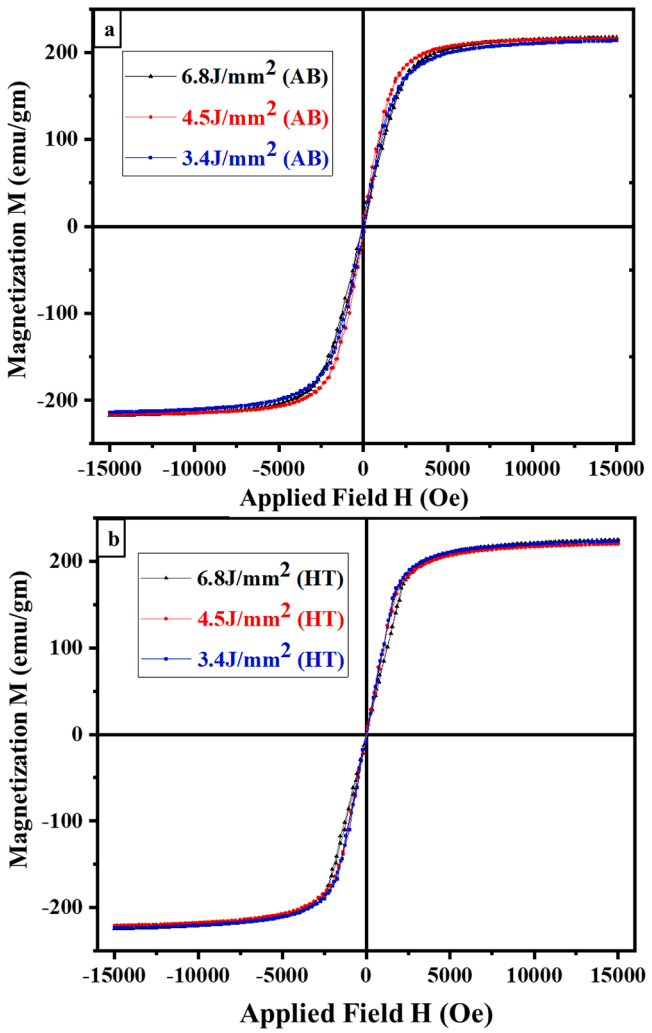

Fig. 4. M-H curves of LPBF Fe-Co-2 V (a) as-built (b) Annealed / Heat-Treated (HT) conditions.

within the parent BCC phase. In contrast, after annealing there appeared strong intense {010} superlattice reflections, marked with a circle in Fig. 5(c). This clearly indicates a higher degree of B2 ordering after annealing. The weak B2 ordering observed in the as built condition is a result of rapid cooling associated with the LPBF processing. The higher degree of B2 ordering in the annealed condition can be attributed to the slower furnace cooling after the 865 °C, 4 h annealing treatment. Furnace cooling resulted in a longer duration for the disordered BCC to ordered B2 transformation to occur at ~500 °C, leading to a higher degree of ordering. Dark-field TEM imaging of the B2 domains was carried out in the case of both the as built and annealed conditions. Figs. 5(b) and (d) display the dark-field (DF) TEM images for the as built and annealed conditions. While the annealed condition (Fig. 5(d)) showed significantly larger scale ordered B2 domains, separated by anti-phase domain (APD) boundaries, in case of the as built condition (Fig. 5 (b)) it is very difficult to discern the domain structure inside the BCC matrix, presumably due to the very early stages of B2 ordering resulting in very fine scale B2 domains. Overall, the M_s values of the annealed conditions range from 228 to 231 emu/g, suggesting the presence of well-developed coarse ordered B2 domains in all the annealed LPBF samples.

Table 1
Magnetic properties of LPBF processed and post heat treated LPBF processed Fe-Co-2 V alloys.

Condition	Laser Fluence (F) (J/mm^2)	Average grain size (μm)	Saturation Magnetization (M_s) (emu/g)	Coercivity (H_c) (Oe)
150 W, 400 mm/s (AB)	6.8	3	217 ± 5	25.8 ± 0.7
150 W, 600 mm/s (AB)	4.5	3	216 ± 3	26 ± 0.5
150 W, 800 mm/s (AB)	3.4	2	213 ± 5	26.5 ± 1
150 W, 400 mm/s (AB) +870C,4 hrs (95 %Ar + 5 % H_2)	6.8	60	228 ± 3	6.9 ± 0.8
150 W, 600 mm/s (AB) +870C,4 hrs (95 %Ar + 5 % H_2)	4.5	60	231 ± 3	8.8 ± 1.2
150 W, 800 mm/s (AB) +870C,4 hrs (95 %Ar + 5 % H_2)	3.4	60	228 ± 5	10.8 ± 0.8

Summary and conclusions

- The average grain size in LPBF processed Hiperco did not show any significant change with the progressive increase in laser scanning speed from 400 mm/s (fluence 6.8 J/mm^2) 600 mm/s (fluence 4.5 J/mm^2) to 800 mm/s (fluence 3.4 J/mm^2). However, the higher cooling rates resulting from the increase in laser scanning speed, resulted in a systematic increase in-grain misorientations, as revealed by EBSD - Kernel Average Misorientation maps, though without any substantial change in the overall average grain size.
- There is a substantial reduction in H_c in the annealed LPBF Fe-49Co-2 V samples as compared to the as-built conditions. On annealing, the H_c of samples built with fluences of 6.4 J/mm^2, 4.5 J/mm^2, and 3.4 J/mm^2 reduced from 25.8 Oe, 26 Oe, and 26.5 Oe to 6.9 Oe, 8.8 Oe, and 10.8 Oe, respectively. The substantial reduction in H_c can be attributed to the high fraction of coarse recrystallized grains (~55 mm) coupled with an increase in the degree of B2 ordering in the annealed samples.
- Annealing also results an increase in the M_s values for samples processed using the three laser fluences. For example, the samples processed using a laser fluence of 3.4 J/mm^2 exhibited an increase in M_s from 213 emu/g to 228 emu/g due to annealing. This increase can be attributed to a higher degree of B2 ordering after annealing (865 °C/4 hrs followed by furnace cooling) as compared to the as built sample. While the as-built condition exhibits a very early stage of B2 ordering, based on the electron diffraction results, annealing followed by slow-cooling results in a well ordered B2 phase with coarse ordered domains, as revealed by dark-field TEM images.

CRediT authorship contribution statement

S.M. Varahabhatla: Writing – review & editing, Investigation, Formal analysis. **V. Chaudhary:** Writing – review & editing, Investigation, Formal analysis. **Abhishek Sharma:** Investigation, Formal analysis. **S.A. Mantri:** Investigation, Formal analysis. **S.S. Joshi:** Investigation, Formal analysis. **R.V. Ramanujan:** Writing – review & editing, Investigation, Formal analysis. **Narendra B. Dahotre:** Writing – review & editing, Investigation, Formal analysis. **R. Banerjee:** Writing – review & editing, Supervision, Resources, Funding acquisition.

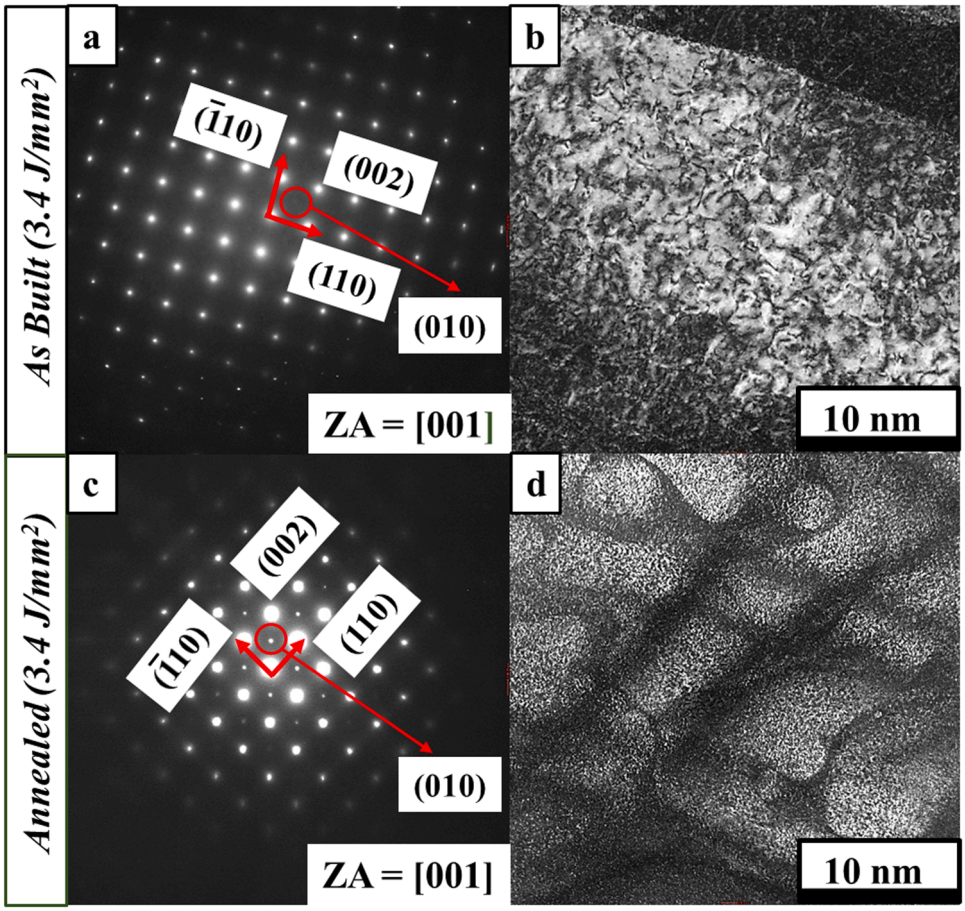

Fig. 5. (a, b) Diffraction pattern and the corresponding dark field image of LPBF 3.4 J/mm^2 as-built condition, (c, d) Diffraction pattern and the corresponding dark field image of LPBF 3.4 J/mm^2 Heat-treated (HT) condition.

Declaration of competing interest

The authors declare that they have no known competing financial interests or personal relationships that could have appeared to influence the work reported in this paper.

Data availability

Data will be made available on request.

Acknowledgements

The authors acknowledge the infrastructure and support of Center for Agile & Adaptive and Additive Manufacturing (CAAAM) funded through State of Texas Appropriation #190405-105-805008-220 and Materials Research Facility (MRF) at the University of North Texas. This work is also supported by the AME Programmatic Fund by the Agency for Science, Technology and Research, Singapore under Grant No. A1898b0043, and Production Area of Advance (AoA) at Chalmers University of Technology.

Supplementary materials

Supplementary material associated with this article can be found, in the online version, at doi:10.1016/j.addlet.2024.100208.

References

[1] S. Li, K.B. Lau, D. Wuu, F. Wei, M. Lin, A. Cheong, P. Wang, C.C. Tan, U. Ramamurty, 3D printing of ductile equiatomic Fe-Co alloy for soft magnetic applications, Addit. Manuf. 47 (2021), https://doi.org/10.1016/j.addma.2021.102291.

[2] K.A. Liogas, K.B. Lau, Z. Wang, D.N. Brown, E. Polatidis, P. Wang, A.M. Korsunsky, Effect of heat treatment on the microstructure and magnetic properties of laser powder bed fusion processed equiatomic Co-Fe, Addit. Manuf. 67 (2023), https://doi.org/10.1016/j.addma.2023.103499.

[3] T.F. Babuska, M.A. Wilson, K.L. Johnson, S.R. Whetten, J.F. Curry, J.M. Rodelas, C. Atkinson, P. Lu, M. Chandross, B.A. Krick, J.R. Michael, N. Argibay, D.F. Susan, A.B. Kustas, Achieving high strength and ductility in traditionally brittle soft magnetic intermetallics via additive manufacturing, Acta Mater. 180 (2019) 149–157, https://doi.org/10.1016/j.actamat.2019.08.044.

[4] T.F. Babuska, K.L. Johnson, T. Verdonik, S.R. Subia, B.A. Krick, D.F. Susan, A. B. Kustas, An additive manufacturing design approach to achieving high strength and ductility in traditionally brittle alloys via laser powder bed fusion, Addit. Manuf. 34 (2020), https://doi.org/10.1016/j.addma.2020.101187.

[5] M.J. Mills, J.L. Biddlecom, B. Pineyro, T.A. Khraishi, S.J. Grutzik, A.R. Brink, M.R. W. Brake, K.L. Johnson, Characterizing the fatigue behavior of wrought Fe–Co–2V using experimental techniques, J. Eng. Mater. Technol. 144 (2022), https://doi.org/10.1115/1.4054142.

[6] T.W. Paplham, D.W. Greve, M.K. Ghosh, L. Wewer, P.R. Ohodnicki, Spatially tuned properties in a bulk Fe–Co soft magnetic alloy via transverse induction annealing and feasibility study for motor applications, Adv. Eng. Mater. (2023), https://doi.org/10.1002/adem.202301363.

[7] R.V. Major, C.M. Orrock, High saturation ternary cobalt-iron based alloys, IEEE Trans. Magn. 24 (1988) 1856–1858, https://doi.org/10.1109/20.11625.

[8] R.H. Yu, S. Basu, L. Ren, Y. Zhang, A. Parvizi-Majidi, K.M. Unruh, J.Q. Xiao, High temperature soft magnetic materials: FeCo alloys and composites, 2000. https://doi.org/10.1109/20.908809.

[9] R.S. Sundar, S.C. Deevi, Soft magnetic FeCo alloys: alloy development, processing, and properties, Int. Mater. Rev. 50 (2005) 157–192, https://doi.org/10.1179/174328005×14339.

[10] T. Sourmail, Near equiatomic FeCo alloys: constitution, mechanical and magnetic properties, Prog. Mater. Sci. 50 (2005) 816–880, https://doi.org/10.1016/j.pmatsci.2005.04.001.

[11] Richard M. Bozorth, Ferromagnetism, 1978. https://ieeexplore.ieee.org/servlet/opac?bknumber=5263070 (accessed January 8, 2024).
[12] G. Herzer, Grain S I Z E Dependence Of Coercivity And Permeability In Nanocrystalline Ferromagnets, 1990. https://doi.org/10.1109/20.104389.
[13] D. Xue, G. Chai, X. Li, X. Fan, Effects of grain size distribution on coercivity and permeability of ferromagnets, J. Magn. Magn. Mater. 320 (2008) 1541–1543, https://doi.org/10.1016/j.jmmm.2008.01.004.
[14] R.H. Yu, S. Basu, Y. Zhang, A. Parvizi-Majidi, J.Q. Xiao, Pinning effect of the grain boundaries on magnetic domain wall in FeCo-based magnetic alloys, J. Appl. Phys. 85 (1999) 6655–6659, https://doi.org/10.1063/1.370175.
[15] R. Alben, J.J. Becker, M.C. Chi, Random anisotropy in amorphous ferromagnets, J. Appl. Phys. 49 (1978) 1653–1658, https://doi.org/10.1063/1.324881.
[16] G. Herzer, Soft magnetic nanocrystalline materials, 1995. https://doi.org/10.1016/0956-716X(95)00397-E.
[17] G. Herzer, Grain structure and magnetism of nanocrystalline ferromagnets, 1989. https://doi.org/10.1109/20.42292.
[18] G. Herzer, Anisotropies in soft magnetic nanocrystalline alloys, J. Magn. Magn. Mater. (2005) 99–106, https://doi.org/10.1016/j.jmmm.2005.03.020.
[19] M.J. Marcinkowski, H. Chessin, Relationship between flow stress and atomic order in the FeCo alloy, Philos. Mag. 10 (1964) 837–859, https://doi.org/10.1080/14786436408225388.
[20] S.T. Fong, M.J. Marcinkowskit, K. Sadananda, Effect of atomic order on slip, twinning and crack formation in FeCo at 4.2°K, 1973. https://doi.org/10.1016/0001-6160(73)90044-8.
[21] L. Zhao, I. Baker, The effect of grain size and fe:Co ratio on the room temperature yielding of FeCo, 1994. https://doi.org/10.1016/0956-7151(94)90020-5.
[22] E.P. George, A.N. Gubbi, I. Baker, L. Robertson, Mechanical properties of soft magnetic FeCo alloys, 2002. https://doi.org/10.1016/S0921-5093(01)01594-5.
[23] C.H. Shang, R.C. Cammarata, T.P. Weihs, C.L. Chien, Microstructure and hall-petch behavior of Fe-Co-based Hiperco alloys, 2000. https://doi.org/10.1557/JMR.2000.0118.
[24] N.E. Fenineche, M. Cherigui, H. Aourag, C. Coddet, Structure and magnetic properties study of iron-based thermally sprayed alloys, Mater. Lett. 58 (2004) 1797–1801, https://doi.org/10.1016/j.matlet.2003.11.009.
[25] S.M. Varahabhatla, M.S.K.K.Y. Nartu, S.A. Mantri, V. Chaudhary, K.V.M. Krishna, S.S. Joshi, R.V. Ramanujan, N.B. Dahotre, R. Banerjee, Influence of energy density on the microstructure, growth orientation, and anisotropy of magnetic properties in additively manufactured Fe-3.8wt%Si transformer steels, Materialia (Oxf) 30 (2023), https://doi.org/10.1016/j.mtla.2023.101854.
[26] N. Giannotta, G. Sala, C. Bianchini, A. Torreggiani, A review of additive manufacturing of soft magnetic materials in electrical machines, Machines 11 (2023), https://doi.org/10.3390/machines11070702.
[27] B.R. Rodriguez-Vargas, G. Stornelli, P. Folgarait, M.R. Ridolfi, A.F. Miranda Pérez, A. Di Schino, Recent advances in additive manufacturing of soft magnetic materials: a review, Materials. (Basel) 16 (2023), https://doi.org/10.3390/ma16165610.
[28] A.B. Kustas, D.F. Susan, K.L. Johnson, S.R. Whetten, M.A. Rodriguez, D.J. Dagel, J. R. Michael, D.M. Keicher, N. Argibay, Characterization of the Fe-Co-1.5V soft ferromagnetic alloy processed by Laser Engineered Net Shaping (LENS), Addit. Manuf. 21 (2018) 41–52, https://doi.org/10.1016/j.addma.2018.02.006.
[29] W. Everhart, J. Newkirk, Grain size effects in selective laser melted Fe-Co-2V,, Appl. Sci. (Switzerland) 9 (2019), https://doi.org/10.3390/app9183701.
[30] S. Firdosy, N. Ury, J.P. Borgonia, B. McEnerney, R. Conversano, R. Hofer, A. Hermann, H. Ucar, V.A. Ravi, R.P. Dillon, Processing–microstructure–property relationships in a laser-deposited Fe-Co-V alloy, Adv. Eng. Mater. 24 (2022), https://doi.org/10.1002/adem.202100931.
[31] T. Riipinen, S. Metsä-Kortelainen, T. Lindroos, J.S. Keränen, A. Manninen, J. Pippuri-Mäkeläinen, Properties of soft magnetic Fe-Co-V alloy produced by laser powder bed fusion, Rapid. Prototyp. J. 25 (2019) 699–707, https://doi.org/10.1108/RPJ-06-2018-0136.
[32] M.S.K.K.Y. Nartu, S. Dasari, A. Sharma, V. Chaudhary, S.M. Varahabhatla, S. A. Mantri, E. Ivanov, R.V. Ramanujan, N.B. Dahotre, R. Banerjee, Reducing coercivity by chemical ordering in additively manufactured soft magnetic Fe–Co (Hiperco) alloys, J. Alloys. Compd. 861 (2021), https://doi.org/10.1016/j.jallcom.2020.157998.
[33] S. Li, K.B. Lau, D. Wuu, F. Wei, M. Lin, A. Cheong, P. Wang, C.C. Tan, U. Ramamurty, 3D printing of ductile equiatomic Fe-Co alloy for soft magnetic applications, Addit Manuf. 47 (2021), https://doi.org/10.1016/j.addma.2021.102291.
[34] Narendra B. Dahotre, Mangesh V. Pantawane, Shashank Sharma, Laser-Based Additive Manufacturing Modeling, Simulation, and Experiments, Wiley, 2022.
[35] M.S.K.K.Y. Nartu, A. Chesetti, S. Dasari, A. Sharma, S.A. Mantri, N.B. Dahotre, R. Banerjee, Engineering heterogeneous microstructures in additively manufactured high entropy alloys for high strength and strain hardenability, Mater. Sci. Eng.: A 849 (2022), https://doi.org/10.1016/j.msea.2022.143505.
[36] M.S.K.K.Y. Nartu, A. Jagetia, V. Chaudhary, S.A. Mantri, E. Ivanov, N.B. Dahotre, R.V. Ramanujan, R. Banerjee, Magnetic and mechanical properties of an additively manufactured equiatomic CoFeNi complex concentrated alloy, Scr. Mater. 187 (2020) 30–36, https://doi.org/10.1016/j.scriptamat.2020.05.063.
[37] R. Ullah, J. Lu, L. Sang, M. Rizwan, Y. Zhang, Z. Zhang, Investigating the microstructural evolution during deformation of laser additive manufactured Ti–6Al–4V at 400 °C using in-situ EBSD, Mater. Sci. Eng.: A 823 (2021), https://doi.org/10.1016/j.msea.2021.141761.
[38] S. Gao, Z. Li, S. Van Petegem, J. Ge, S. Goel, J.V. Vas, V. Luzin, Z. Hu, H.L. Seet, D. F. Sanchez, H. Van Swygenhoven, H. Gao, M. Seita, Additive manufacturing of alloys with programmable microstructure and properties, Nat. Commun. 14 (2023), https://doi.org/10.1038/s41467-023-42326-y.
[39] M. Godec, S. Zaefferer, B. Podgornik, M. Šinko, E. Tchernychova, Quantitative multiscale correlative microstructure analysis of additive manufacturing of stainless steel 316L processed by selective laser melting, Mater. Charact. 160 (2020), https://doi.org/10.1016/j.matchar.2019.110074.